

Modular Approach to Creating Functionalized Surface Arrays of Molecular Qubits

Lorenzo Tesi,* Friedrich Stemmler, Mario Winkler, Sherri S. Y. Liu, Saunak Das, Xiuming Sun, Michael Zharnikov, Sabine Ludwigs, and Joris van Slageren*

The quest for developing quantum technologies is driven by the promise of exponentially faster computations, ultrahigh performance sensing, and achieving thorough understanding of many-particle quantum systems. Molecular spins are excellent qubit candidates because they feature long coherence times, are widely tunable through chemical synthesis, and can be interfaced with other quantum platforms such as superconducting qubits. A present challenge for molecular spin qubits is their integration in quantum devices, which requires arranging them in thin films or monolayers on surfaces. However, clear proof of the survival of quantum properties of molecular qubits on surfaces has not been reported so far. Furthermore, little is known about the change in spin dynamics of molecular qubits going from the bulk to monolayers. Here, a versatile bottom-up method is reported to arrange molecular qubits as functional groups of self-assembled monolayers (SAMs) on surfaces, combining molecular self-organization and click chemistry. Coherence times of up to 13 μs demonstrate that qubit properties are maintained or even enhanced in the monolayer.


1. Introduction

Quantum technologies are set to go beyond current methods for performing large-scale computations and of resolving

L. Tesi, F. Stemmler, M. Winkler, J. van Slageren
Institute of Physical Chemistry and Center for Integrated Quantum
Science and Technology
University of Stuttgart
Pfaffenwaldring 55 70569, Stuttgart, Germany
E-mail: lorenzo.tesi@ipc.uni-stuttgart.de; slageren@ipc.uni-stuttgart.de

S. S. Y. Liu, X. Sun, S. Ludwigs
IPOC-Functional Polymers
Institute of Polymer Chemistry and Center for Integrated Quantum
Science and Technology
University of Stuttgart
Pfaffenwaldring 55 70569, Stuttgart, Germany

S. Das, M. Zharnikov
Applied Physical Chemistry
Heidelberg University
Im Neuenheimer Feld 253 69120, Heidelberg, Germany

 The ORCID identification number(s) for the author(s) of this article can be found under <https://doi.org/10.1002/adma.202208998>.

© 2023 The Authors. Advanced Materials published by Wiley-VCH GmbH. This is an open access article under the terms of the Creative Commons Attribution License, which permits use, distribution and reproduction in any medium, provided the original work is properly cited.

DOI: 10.1002/adma.202208998

quantum physics and chemistry problems.^[1] For this purpose, researchers world-wide are devoting their efforts to the development of quantum computing, quantum simulations and quantum sensing.^[2] The benefits of this technology could potentially help to solve high-impact problems such as understanding high temperature superconductivity, further miniaturization of transistors in processors, and the prediction of properties of novel pharmaceuticals.^[3–5] The fundamental unit for quantum applications is the quantum bit or qubit, which in general terms is a system with two or more levels that can be put into coherent superposition states for a limited time, called coherence time.^[6] Several systems are currently being investigated as qubits, linking their properties to specific applications: photons for quantum communication,^[7] superconducting circuits for

quantum computing,^[8,9] and nitrogen vacancies in diamonds for quantum sensing of magnetic fields.^[10,11] Other interesting platforms include phosphorous impurities in silicon,^[12] quantum dots,^[13] Rydberg atoms^[14] and trapped ions.^[15,16] All these potential qubit platforms exhibit remarkable properties when working as individual units. However, the coupling of several of these units, required for the realization of quantum gates, is challenging. Similarly, their scalability is limited by the lack of a manufacturing process that enables accurate qubit positioning in arrays.^[17] Both these requirements must be fulfilled to achieve a working quantum device, which is thus a nontrivial task. Molecular spin qubits (MSQs) are a promising platform that would allow addressing these challenges.^[18–23] Molecules are microscopic quantum objects, like atoms but more versatile in their composition, with a high potential to form ordered structures at the nanoscale.^[24,25] Thanks to their synthetic versatility, it is possible to fine-tune the interaction between multiple qubits^[26–28] and to modify the ligand shell to meet specific practical demands, for example for transferring qubits onto a solid substrate or into a device.^[4,29–32] The interest toward MSQs has grown quickly and remarkable results concerning the understanding of the relationship between chemical design and quantum properties have been achieved in a short time.^[33–41] It is now clear that long coherence times can be achieved^[42–45] and that multi spin-level systems can be designed, thanks to which quantum gate

operations and quantum error correction algorithms can be implemented even in individual molecules.^[46–52] These studies were conducted mainly on bulk systems such as crystals, powders and solutions. However, the integration of MSQs in circuits and devices requires arranging them on surfaces.^[53–57] Such a drastic modification of the system character, going from the bulk to a surface, can result in a significant change of the qubit properties. Above all, reaching the next level in the development of quantum devices requires the experimental demonstration that MSQs are still functional once deposited on a surface, for example as self-assembled monolayers (SAMs). To this end, it is of fundamental importance to develop a deposition method that does not affect the coherence times. In this regard, a study by Poggini et al. is noteworthy, where the authors investigated, both experimentally and theoretically, a thiol-functionalized nitroxyl nitroxide radical directly grafted to a gold surface.^[58] The authors concluded that the molecules connected to the surface prefer a laid-down orientation rather than a stand-up geometry. Consequently, the π^* -orbitals of the NO radical groups coupled strongly with the electronic states of the substrate with a consequent partial delocalization of the spin density across the interface, with detrimental results for the coherence times. A similar conclusion was also drawn by Rajaraman et al.^[59] Hence, to preserve quantum coherence, one needs to efficiently decouple the radical groups from the substrate. Other SAMs of radical species have been reported as well but their spin dynamics were not investigated.^[60–63] At the same time, it is necessary to identify experimental techniques capable of measuring the spin dynamics of samples containing a small number of spins, as in the case of thin films or monolayers, ideally without having to process the layers after deposition, e.g., by cutting the sample into smaller pieces.

In this work, we address these two issues. First, we present a strategy for depositing the qubits on surfaces without losing their functionality. To this end, we use a two-step modular approach relying on click chemistry, illustrated in **Figure 1**. In the first step, the gold substrate (a thin film on Kapton) is functionalized with an azide-substituted alkanethiolate SAM that serves as linker for the radical moieties. Subsequently, in the

second step, a derivative of the TEMPO (2,2,6,6-tetramethylpiperidine-1-oxyl) radical is attached to the SAM, exploiting the Huisgen reaction between the apex azide group of the linker and the terminal alkyne group of the radical moiety (click reaction). In this way, the alkane backbone of the SAM acts as a spacer and decouples the radical from the surface. Second, using a specifically designed electron paramagnetic resonance (EPR) resonator, we demonstrate full functionality of the deposited qubit array, finding coherence times of up to 13 μ s at temperatures between 10 and 60 K. Surprisingly, these times are even longer than the respective bulk values for the TEMPO-derivative used, especially considering that the qubits in the SAM are not diluted.

2. Results

2.1. Sample Preparation

A SAM of 11-azidoundecane-1-thiol (11AU1T) on gold was prepared by submerging a clean gold substrate (50 nm gold on Kapton) in a 1×10^{-3} M solution of 11AU1T in ethanol for 2 days in the dark and under an inert atmosphere (Figure 1b).^[64] The resulting 11AU1T SAM was washed with ethanol under sonication to remove physisorbed species from the surface. Afterward, this SAM was reacted for six days with PTEMPO (4-propargyl-2,2,6,6-tetramethylpiperidine-1-oxyl) in dry THF, using CuI/triethylamine/TBTA (tris[(1-benzyl-1H-1,2,3-triazol-4-yl)methyl]amine) as catalyst in a Huisgen 1,3-dipolar cycloaddition click reaction.^[65,66] The TEMPO radical was chosen in view of its characteristic EPR spectrum that allows monitoring its properties after the monolayer formation. Moreover, TEMPO has reasonable spin relaxation times in diluted solution to potentially work as a qubit.^[67,68] The resulting TEMPO SAM was washed with anhydrous THF under sonication and then placed in vacuo. The root mean square roughness of the pristine substrate determined by atomic force microscopy (AFM) changed from 1.1(2) nm to 1.7(2) nm after the TEMPO SAM preparation, in agreement with a modification of the surface.

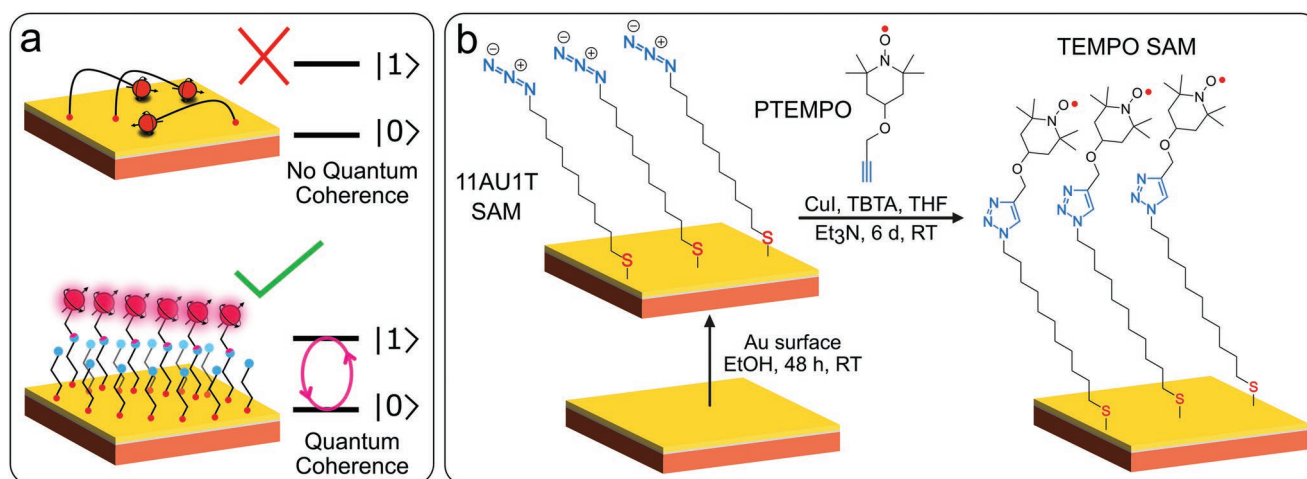


Figure 1. a) Conceptual experimental scheme: the method described in this work allows creating an ordered 2D array of qubits on surface, which retains their quantum properties. b) Two-step strategy for assembling TEMPO on gold surface. In the first step, the 11AU1T linker is chemisorbed on the surface. In the second step, the PTEMPO is chemically connected to the linker via click chemistry.

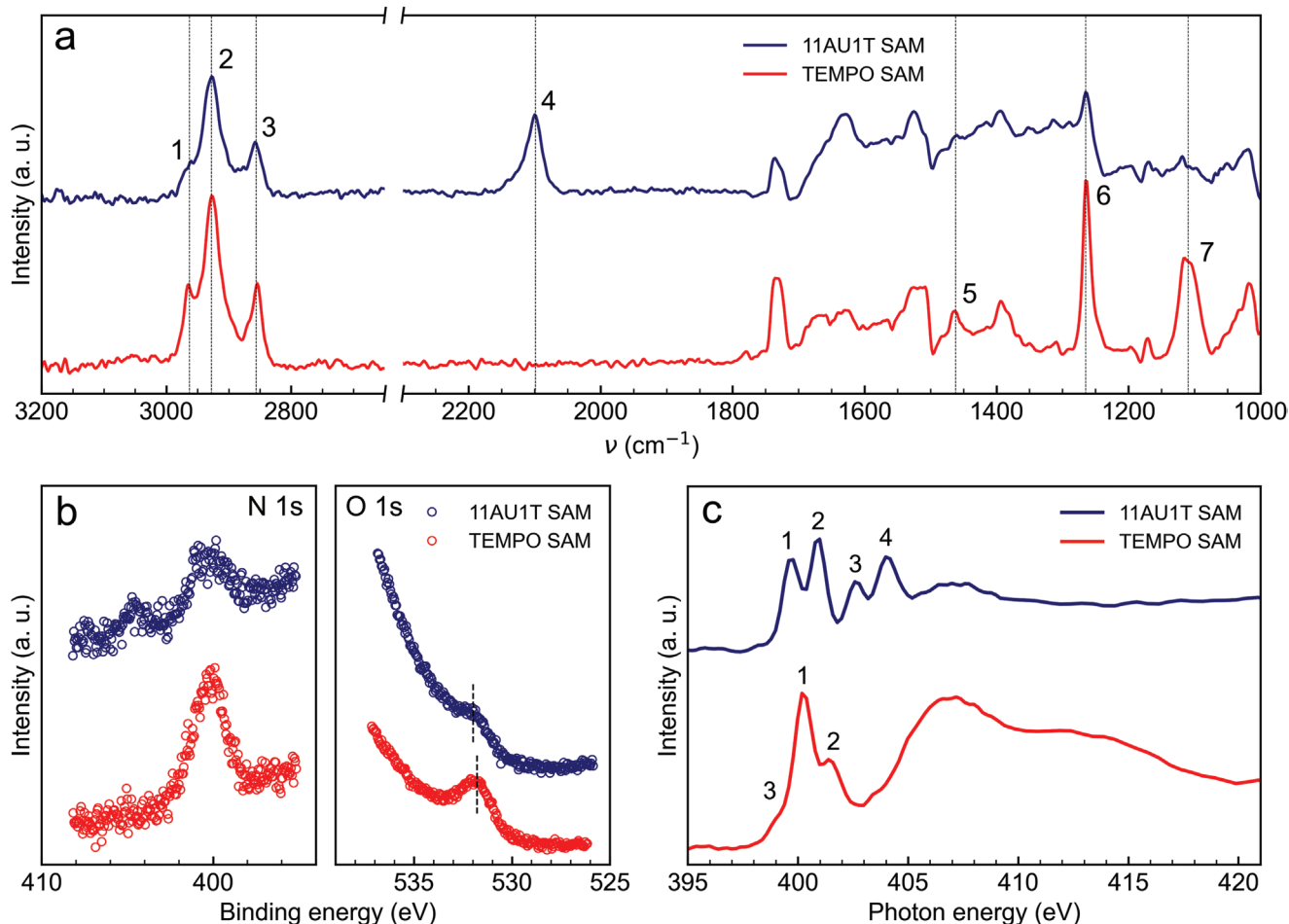


Figure 2. a) PM-IRRAS spectra of the 11AU1T and TEMPO SAMs. The vertical dashed lines indicate the most prominent vibration bands. b) N 1s and O 1s XPS spectra of the 11AU1T and TEMPO SAMs. The photon energy was 580 eV. The dashed lines in the O 1s spectra indicate the positions of the maxima. c) N K-edge NEXAFS spectra of the 11AU1T and TEMPO SAMs. The X-ray incidence angle was set to 55°. Characteristic absorption resonances are marked by numbers (see text).

2.2. Spectroscopic Characterization of the Monolayer

The formation of the 11AU1T SAM and its subsequent functionalization with PTEMPO were investigated by surface-sensitive polarization modulation infrared reflection absorption spectroscopy (PM-IRRAS), X-ray photoelectron spectroscopy (XPS), and near-edge X-ray absorption fine structure (NEXAFS) spectroscopy. The PM-IRRAS spectrum of the 11AU1T SAM (Figure 2a) shows a distinct peak at 2099 cm^{-1} (peak 4) characteristic of the azido stretching vibration $\nu(\text{N}_3)$. This peak is absent in the spectrum of the TEMPO SAM, demonstrating that all azide groups have reacted with PTEMPO and hence that the functionalization reaction was complete. In the aliphatic stretching region between 3000 and 2800 cm^{-1} , the characteristic asymmetric and symmetric methylene stretching bands at $\approx 2926 \text{ cm}^{-1}$ (peak 2) and $\approx 2854 \text{ cm}^{-1}$ (peak 3), respectively, were observed, with the intensity ratio typical of alkanethiolate SAMs on Au(111). The positions of these bands are somewhere between those for all-trans conformation of the alkyl backbones (2920 cm^{-1} and 2852 cm^{-1})^[69,70] and those of liquid alkane (2928 cm^{-1} and 2856 cm^{-1})^[70] that has $\approx 40\%$ C—C gauche conformations. Thus, the 11AU1T SAM contained a certain degree

of conformational disorder, which stemmed most likely from the presence of the azide groups but did not affect the performance of this monolayer in context of the click reaction. The successful character of this reaction is further corroborated by the clear signatures of PTEMPO, viz. the $\nu(\text{N—O})$ and $\nu(\text{C—O})$ bands at 1462 (peak 5) and 1100 cm^{-1} (peak 7), respectively, as well as by the appearance of the bands at 1260 (peak 6) and 1110 cm^{-1} (peak 7) that are a mixture of vibrational modes of the triazole ring formed after the click reaction (see Figure 1b).^[71] The absence of a $\nu(\text{C—C})$ peak at 2130 cm^{-1} indicates that the amount of physisorbed species is negligible. Finally, the spectrum of the TEMPO SAM shows a clear signal due to the $\nu(\text{CH}_3)$ vibration at 2965 cm^{-1} (peak 1), which was very weak in the 11AU1T spectrum.

The N 1s and O 1s XPS spectra of the 11AU1T and TEMPO SAMs are presented in Figure 2b. The N 1s spectrum of the 11AU1T SAM exhibits the characteristic features of the azide group,^[64,72] viz. the peaks at 400.4 and 404.6 eV, with the intensity ratio close to 2. This spectrum changed radically upon the attachment of TEMPO, showing only one peak at 400.1 eV, characteristic of 1,2,3-triazole^[64] linking the aliphatic chain to the TEMPO moiety after the click reaction (see Figure 1b).

The signal from the nitrogen atom of TEMPO most likely overlaps with this peak, which is indirectly supported by the higher intensity of the joint feature compared to that for the 11AU1T SAM as well as to the intensity of the analogous feature after the click reaction of a reference compound, 1-ethynyl-3,5-bis(trifluoromethyl)benzene (Figures S1 and S2, Supporting Information). The O 1s spectrum of the 11AU1T SAM in Figure 2b exhibits a weak, asymmetric peak at ≈ 532.0 eV, stemming most likely from a minor contamination. This spectrum changed noticeably upon the attachment of TEMPO, showing a well-defined peak at ≈ 531.8 eV, assigned to the O atom of the TEMPO moiety. The strongest evidence of the successful character and completeness of the click reaction is provided by the NEXAFS data, which are presented in Figure 2c. Note that the respective spectra were acquired at the so-called magic angle of X-ray incidence (55°) to avoid any effects of molecular orientation. Accordingly, they are exclusively representative of the electronic structure of the SAMs studied.^[73] The N K-edge NEXAFS spectrum of the 11AU1T SAM exhibits the characteristic π^* -resonance pattern of the intact azide group,^[64,74] viz. the resonances at 399.7 eV (peak 1), 400.9 eV (peak 2), 402.6 eV (peak 3), and 404 eV (peak 4), with the characteristic intensity relations between the individual features. This pattern originates from a superposition of two different charging configurations of the azide group^[74] and represents, thus, its distinct signature. This signature disappeared completely upon the attachment of TEMPO, and a new π^* -resonance pattern, characteristic of 1,2,3-triazole,^[74] emerged. This pattern is represented by the dominant resonance at 400.25 eV (peak 1), accompanied by a weaker resonance at ≈ 401.5 eV (peak 2) and a low intense shoulder at ≈ 398.8 eV (peak 3).

Summarizing, the PM-IRRAS, XPS, and NEXAFS spectroscopy data provide strong and consistent evidence for the formation of the azide-terminated 11AU1T SAM as well as the successive coupling of the TEMPO moieties to the terminal azide groups of this SAM by the click reaction. Significantly, the characteristic spectroscopic features of the azide group appear exactly as expected, which would be hardly the case if they interact with the substrate, resulting in a significant quenching of the characteristic NEXAFS resonances. Thus, the azide groups are electronically decoupled from the substrate, transferring this useful property to the attached TEMPO moieties. Significantly, the extent of the click reaction is close to 100%, so that all these moieties represent the terminal groups of the modified SAM, building a well-defined 2D array of qubits, connected to the substrate by the aliphatic linkers. The density of the qubits is expected to mimic that of the 11AU1T template. The latter can be assumed to be close to the packing density of standard alkanethiolate SAMs on Au(111), viz. 4.63×10^{14} molecules cm^{-2} ,^[75] or somewhat lower than this value in view of a certain degree of conformational disorder in the 11AU1T SAM. To investigate the coverage, we have carried out cyclic voltammetry experiments at different scan speeds (Figure S3, Supporting Information). The peak current dependence on scan speed is linear as expected for surface-immobilized species. On the basis of the CV curves, the coverage was estimated to be $4(2) \times 10^{14}$ molecules cm^{-2} (details in the Supporting Information), which is in line with the value assumed above.

2.3. Continuous-Wave EPR

Having ascertained the successful preparation of the TEMPO SAM, the next step was to demonstrate the chemical and physical intactness of the functional units, i.e., the TEMPO-based qubits. Continuous-wave (CW)-EPR spectroscopy is the most suitable technique for this purpose. Indeed, TEMPO has a distinct EPR spectrum, due to the highly anisotropic hyperfine coupling between the electron spin and the $I = 1$ ^{14}N nuclear spin. This signature allows assigning the spectra unequivocally to TEMPO and allows excluding surface defects and paramagnetic impurities. Furthermore, the CW-EPR spectrum of TEMPO is very sensitive to the motional dynamics of the TEMPO moiety and intermolecular spin-spin interactions between individual moieties.^[67] To obtain sufficient signal-to-noise ratio, four TEMPO SAM functionalized Kapton stripes were placed in an X-Band EPR tube and measured both at room temperature and at 100 K. For purposes of comparison, a solution of PTEMPO 1×10^{-3} M in 1:1 dichloromethane/toluene was measured at the same temperatures, i.e., as fluid and frozen solutions, respectively. The EPR spectra were simulated using the following spin Hamiltonian

$$\mathcal{H} = \mathcal{H}_{\text{EZ}} + \mathcal{H}_{\text{NZ}} + \mathcal{H}_{\text{HF}} = \mu_{\text{B}} \hat{\mathbf{S}} \cdot \mathbf{g} \cdot \mathbf{B} - g_{\text{N}} \mu_{\text{N}} \hat{\mathbf{I}} \cdot \mathbf{B} + \hat{\mathbf{S}} \cdot \mathbf{A} \cdot \hat{\mathbf{I}} \quad (1)$$

The first two terms in Equation (1) correspond to the electronic and nuclear Zeeman splittings whose magnitude depends on i) the \mathbf{g} -tensors, ii) the Bohr and nuclear magneton constants, μ_{B} and μ_{N} , iii) the spin operators, $\hat{\mathbf{S}}$ and $\hat{\mathbf{I}}$, and iv) the applied static magnetic field \mathbf{B} . The last term of the spin Hamiltonian accounts for the hyperfine interaction of the electron and nuclear spins with \mathbf{A} being the hyperfine coupling tensor. The 100 K spectrum of the TEMPO SAM (Figure 3a) displays the typical three-line pattern (up-derivative-down) belonging to a $S = 1/2$, $I = 1$ species with hyperfine splitting, such as TEMPO. Simulations of the spectra on the basis of Equation (1) yielded the spin Hamiltonian parameters reported in Table S1 (Supporting Information). The \mathbf{g} - and \mathbf{A} -values correspond to those reported for TEMPO species (see below), and therefore this observation unambiguously demonstrates the intactness of the TEMPO groups in the SAM. Indeed, the spectrum is virtually identical to that of the frozen solution of PTEMPO at 95 K. In contrast, the fluid solution spectrum recorded on PTEMPO (Figure 3a) displays three equal lines with equal intensities, where the splitting is again due to hyperfine coupling between the electron spin and the ^{14}N nuclear spin. Here, the anisotropy is averaged out due to fast tumbling of the molecules in fluid solution, corresponding to a small rotational correlation time τ_c (9.5 ps). Interestingly and in contrast to the change observed for PTEMPO, the room temperature spectrum of the TEMPO SAM is almost equal to the spectrum recorded at 100 K, indicating limited mobility of the TEMPO moieties in the SAM. This behavior is likely a combined effect of covalent bonding of the TEMPO groups to the alkanethiolate linkers and their close packing in the confined 2D array limiting their motional degrees of freedom.^[76] However, a small but significant difference in the spectrum of TEMPO SAM at room temperature is the presence of two extra EPR lines at intermediate magnetic fields, viz. at 335 and 339 mT. To simulate the spectrum of

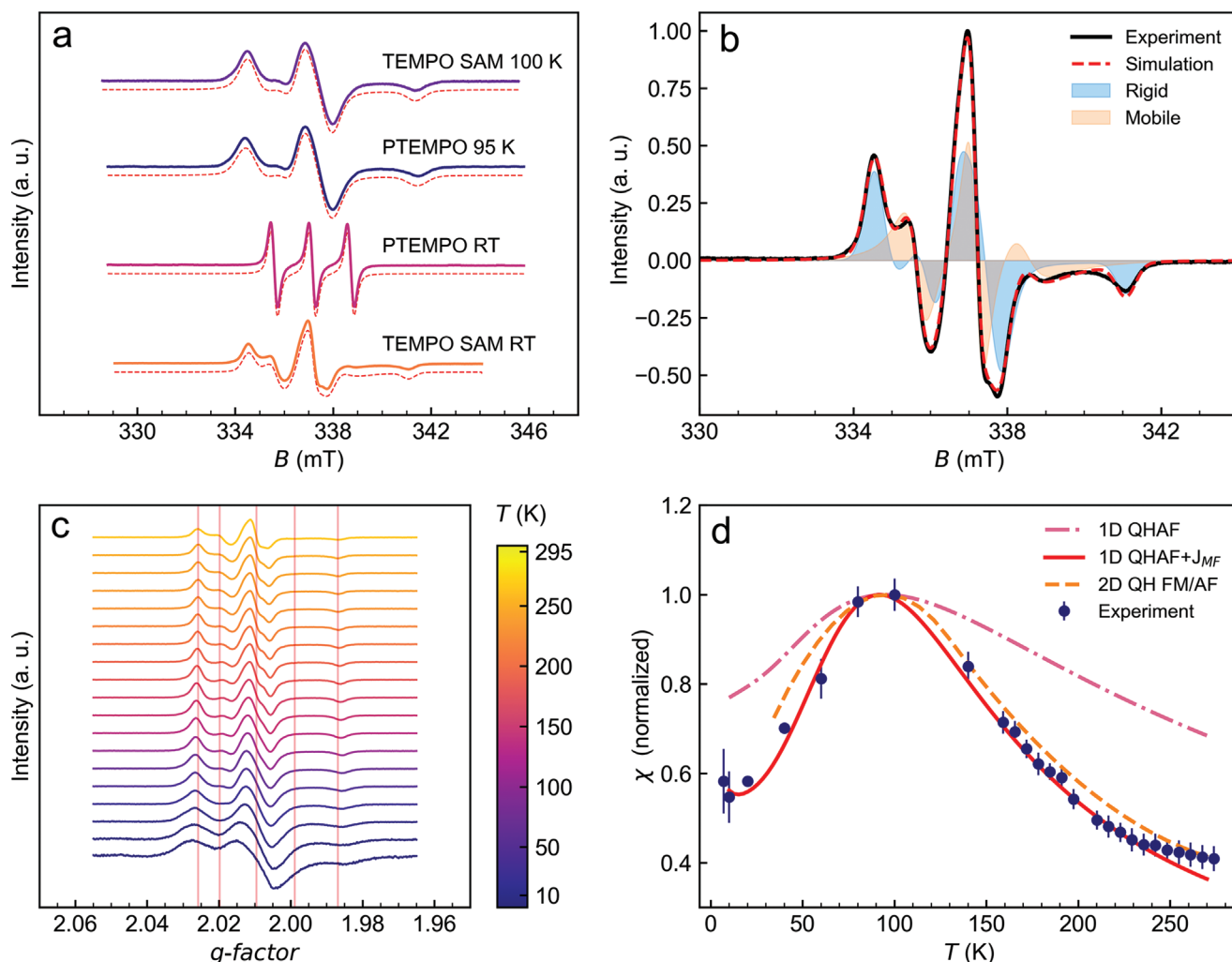


Figure 3. a) Experimental and simulated X-Band CW-EPR spectra of the TEMPO SAM at room temperature and 100 K and the spectra of 1×10^{-3} M PTEMPO DCM:toluene (1:1) solution at room temperature and 95 K (solid lines), and corresponding fits (red dashed lines). b) Experimental and simulated X-Band CW-EPR spectra of the TEMPO SAM at room temperature. The simulation is performed considering two components, one rigid and another quasi-mobile, that have $\approx 50:50$ weights and are displayed as well. c) Normalized experimental X-Band CW-EPR spectra of the TEMPO SAM at temperatures from 7 to 295 K. The spectra are presented in a stack plot. The vertical red lines are guides to the eye to highlight the shift of the peaks occurring with temperature. d) Temperature dependence of χ obtained by double integration of the experimental EPR spectra of the TEMPO SAM. The pink point-dashed line is the best simulation using the 1D QHAF model. The red solid line corresponds to the same model with the inclusion of a ferromagnetic mean field interaction and a contribution of 1% non-interacting spins, which results in the increasing of χ from 10 to 7 K. The orange dashed line is the 2D QH FM/AF model for $J_{AF} = -0.1 J_{FM}$ obtained by Quantum Monte Carlo calculations and reported by Keith et al.^[10]

TEMPO SAM at room temperature (Figure 3b), it proved to be necessary to introduce two components, viz. one corresponding to a motionally rigid species ($\tau_c = \infty$) and a second one that is somewhat mobile ($\tau_c = 2$ ns from the simulations). The parameters used for simulating the room temperature EPR spectrum of the TEMPO SAM are reported in Table S2 (Supporting Information) and they are in accordance with the values obtained for PTEMPO (Table S1, Supporting Information). The relative contribution of both components is $\approx 50:50$. By dipping the TEMPO SAM into toluene to increase mobility, an increase of the intensity of the lines relative to the quasi-mobile species was observed, while upon subsequent drying of the sample, the spectrum reverted to the original shape (Figure S4, Supporting Information). The occurrence of mobility of nitroxide deriva-

tive SAMs has been reported in several cases together with the absence of a preferential magnetic orientation.^[62,77] Although mobility could be attributed to some degree of disorder in the monolayer, its presence does not preclude local ordering, as pointed out by Mannini et al. on the basis of scanning tunneling microscopy data.^[62,78]

The close packing of the molecules within the 2D array might promote noticeable intermolecular interactions. To investigate this issue, X-Band CW-EPR spectra of TEMPO SAM were recorded from room temperature down to 7 K (Figure 3c). On decreasing the temperature, the normalized spectra as a function of the g -factor display a decrease of the relative intensity of the resonance lines corresponding to the quasi-mobile species. Moreover, there is a progressive line broadening and a significant shift of the lines of

the rigid species (see vertical lines in Figure 3c). The double integral of the spectra, which is reported as a function of temperature in Figure 3d, is proportional to the magnetic susceptibility, χ . Starting from the lowest temperature, χ slightly decreases with increasing temperature and then it strongly increases reaching the maximum at 100 K, after which it decreases again. For a non-interacting spin system, χ should be inversely proportional to the temperature, which is obviously not the case here. At first sight, the observed behavior of χ suggests the presence of a non-negligible antiferromagnetic exchange interaction between the TEMPO groups. However, considering the spin-Hamiltonian term for the exchange coupling, $\mathcal{H} = \sum_{ij} J_{ij} S_i \cdot S_j$, simulations show that neither antiferromagnetic dimeric interactions, nor purely antiferromagnetic (AF) spin-chain interactions lead to faithful reproduction of the experimental data (Figure 3d). Instead, the inclusion of a ferromagnetic (FM) interchain mean-field (MF) interaction of $J_{MF}/k_B \approx -500$ K to the 1D quantum Heisenberg antiferromagnetic (QHAF) model, with $J_{AF}/k_B \approx 100$ K, reproduces the experimental susceptibility rather well (Equation (S1), Supporting Information, and Figure 3d). Note, however, that this model should be considered just as an indication, because, as reported by Johnston et al., the addition of a mean-field term is very accurate only for $|J_{MF}/J| \ll 1$.^[79] Unfortunately, for 2D interactions no parametric or analytical formulas are available. Further evidence of the coexistence of competing interactions is given by the comparison to the simulated curves for a QH magnetic square lattice of antiferro- and ferromagnetic interactions in the two-dimensions obtained by Monte Carlo simulations, and reported in literature.^[80] The closest correspondence is found for dominant ferromagnetic interactions in one direction and weaker antiferromagnetic interactions in the other (QH FM/AF type) with $J_{AF} = -0.1 J_{FM}$, as shown in Figure 3d. The strength of the exchange coupling can be estimated from comparing the positions of the maxima for the simulated and experimental curves, which gives $J/k_B \approx -600$ K. This value agrees well with the estimate by the QHAF + J_{MF} model, providing additional evidence of substantial exchange interactions in the TEMPO SAM due to the close packing of the radicals. At the lowest temperatures, an upturn in the signal intensity is observed, which we attribute to a small fraction ($\approx 1\%$) of the radicals that are not exchange-coupled. Although a mixed antiferro- and ferromagnetic character was already found in ab initio calculations for nitroxyl nitroxide radicals directly grafted on a gold surface,^[59] further studies on the TEMPO SAM are necessary to confirm the nature and strength of the interactions composing such a complicated network. Nevertheless, we can discuss qualitatively how the EPR spectrum of TEMPO should be modified by sizable exchange interactions: For a dimer of two spins $1/2$, exchange coupling leads to singlet and triplet states, which are the ground states in case of antiferromagnetic or ferromagnetic exchange interaction, respectively. In the strong interaction regime, i.e., at $J \gg A$, the hyperfine coupling of two $I = 1$ nuclear spins leads to a quintet splitting of the EPR spectrum with a 1:2:3:2:1 intensity ratio, but with distances that are halved,^[81] in clear contrast to what is observed here. However, it has been reported that time-dependent modulation of J changes this intensity pattern in such a way that the second and fourth lines are severely broadened and, essentially, the original spectrum is largely recovered.^[82–84] This effect leads to a qualitative agreement with the spectrum of the TEMPO SAM at room

temperature (Figure 3b), which shows a quintet splitting where the second and fourth lines (at 335 and 339 mT) have much weaker intensities than the external and central lines. Thus, potentially, the dimer scenario with time-dependent J could be extended to the 2D arrangement of radicals in the TEMPO SAM sample. Accordingly, the second and fourth lines are not due to a second (quasi-mobile) species as hypothesized above. One argument against this scenario is that the weak lines progressively disappear as the temperature is decreased (Figure 3c). In contrast, if the time-dependent J -modulation scenario would be valid, the expected reduced mobility at lower temperature would decrease the J -modulation and thus, additional lines should appear. A second scenario follows the biradical paradox, where “monomeric” EPR spectra are observed for biradicals with reasonably strong intramolecular exchange interactions. These observations have been explained in terms of strong intermolecular interactions in a chain-like fashion, leaving only the spins at the extreme of the chain to contribute to the EPR spectrum.^[85] This could be in agreement with what we observe, if the weak, J_{AF} , and the strong, J_{FM} , interactions in the 2D interaction model discussed above correspond respectively to the intramolecular and intermolecular interactions of the biradical model. On the other hand, in the biradical model, the intermolecular interactions should be both antiferromagnetic, which is not what we found from the intensity analysis of χ . Clearly, the issue requires more study to be resolved completely.

2.4. Spin Dynamics

Having established the integrity of the TEMPO SAM qubit array, we now turn to the investigation of the qubit functionality, i.e., the demonstration of quantum coherence in the array. To this end, the spin dynamics of the TEMPO SAM was investigated by means of pulsed EPR at Q-Band frequencies. Here, we have employed a home-built Fabry–Pérot resonator, which was specially designed for the study of flat samples such as thin layers and monolayers, including the present TEMPO SAM in particular.^[86,87] Figure 4a shows the experimental and simulated (Table S3) electron spin echo (ESE)-detected EPR spectrum recorded at 7 K on a sample consisting of four 7×7 mm² squares of the TEMPO SAM. The observation of a strong spin echo in this sample immediately proves that quantum coherence is maintained in the qubit array, and thus the main goal of the study was achieved. The shape of the spectrum is identical to that recorded on a frozen solution sample of 1×10^{-3} M PTEMPO in DCM:toluene (1:1) at 7 K (Figure 4a), corroborating the integrity of the TEMPO units and demonstrating unambiguously that the signal is due to the TEMPO SAM rather than to the substrate or paramagnetic impurities. To clarify whether the signal is coming from the entire sample, i.e., the interacting radical molecules, or from the 1% of non-interacting molecules observed by CW-EPR, the minimum number of detectable spins previously determined for this resonator is compared to the number of spins in the sample. Indeed, the sensitivity of the Fabry–Pérot resonator was estimated to be of the order of 10^{11} spins/G $\cdot\sqrt{\text{Hz}}$ at 7 K, with a minimum number of detectable spins of $\approx 1 \times 10^{14}$.^[86] Considering that the investigated TEMPO SAM sample contains an estimate of $8(4) \times 10^{14}$ spins, based on the CV measurements, this result indicates that we are close to the sensitivity limit of the resonator. Therefore, we can conclude that the

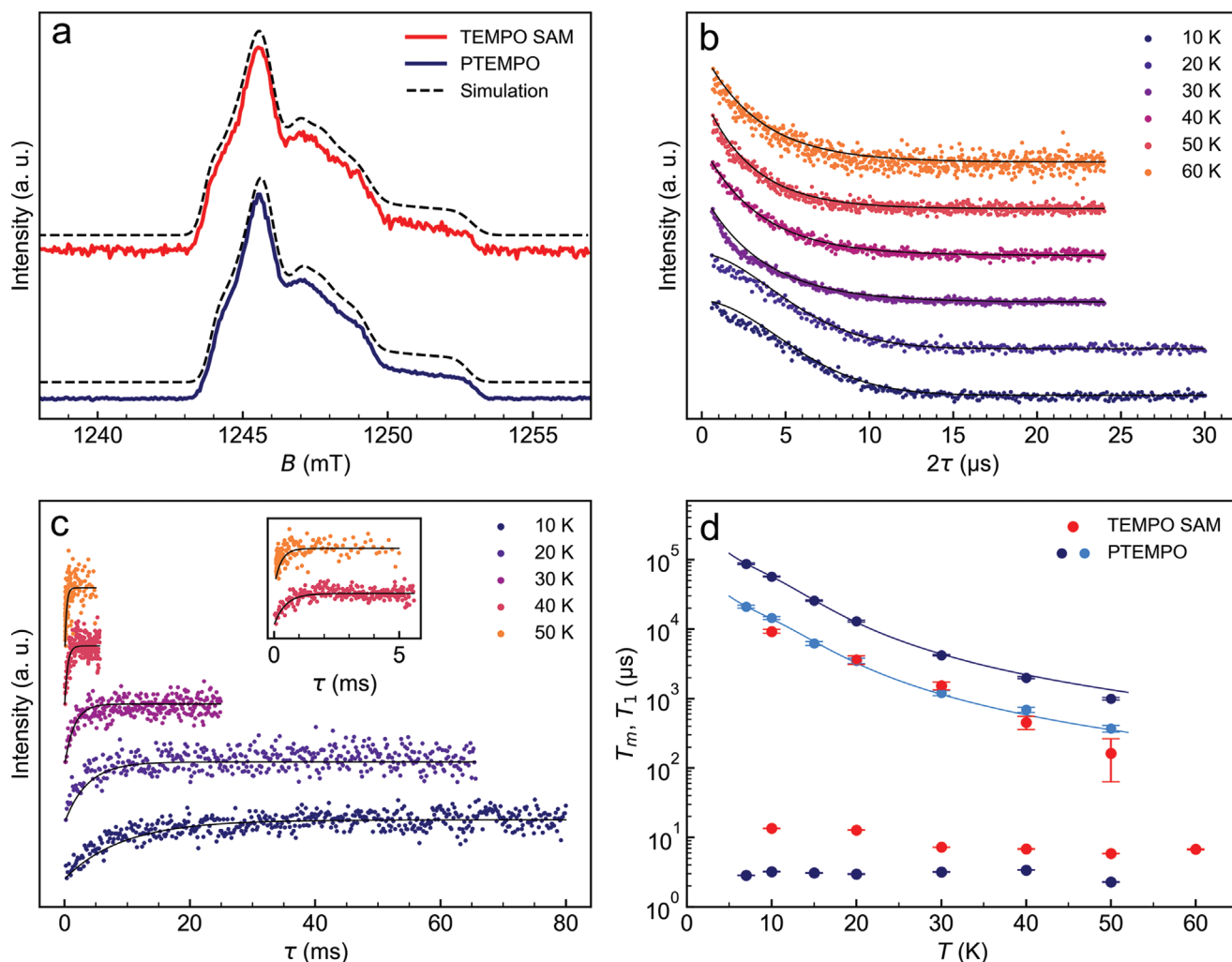


Figure 4. a) Experimental and simulated Q-Band echo-detected pulsed EPR spectra of the TEMPO SAM measured at 7 K with a home-built Fabry–Pérot resonator and of PTEMPO in solution DCM:toluene (1:1) at 7 K. b) Experimental Hahn echo decays for the TEMPO SAM, shown in a stack plot. The solid lines are the best-fits. c) Experimental inversion recovery curves for the TEMPO SAM measured at various temperatures and shown in a stack plot. The solid lines are the best-fits. d) Experimental (dots) and fit (solid lines) temperature dependence of the spin–lattice relaxation time T_1 and phase memory time T_m for the TEMPO SAM and PTEMPO.

signal measured by pulsed EPR involves the entire spin ensemble, rather than a small impurity.

Investigation of spin dynamics in the TEMPO SAM involved the measurement of the phase memory time, T_m , which is the lower experimental limit of the true quantum coherence time, as well as of the spin–lattice relaxation time, T_1 . These measurements were carried out at the field position corresponding to the maximum in the spectrum and at different temperatures. T_m values were determined by using a Hahn echo sequence varying the inter-pulse delay time τ (Figure 4b). The experimental curves at 10 and 20 K were fitted by a stretched exponential decay function (Equation (2)), while for the other temperatures a monoexponential model was adopted

$$I(2\tau) = I(0) \exp \left[- \left(\frac{2\tau}{T_m} \right)^x \right] \quad (2)$$

where I is the echo intensity, 2τ is the inter-pulse time in the Hahn echo sequence and x is the stretch factor. At 10 K, T_m was determined to be $T_m = 13.53(7) \mu\text{s}$ slowly decreasing to $\approx 6 \mu\text{s}$ at 60 K (Figure 4d and Table 1). The stretch factor was ≈ 1.8 at low temperatures decreasing to 1 above 20 K (Table 1). The spin–lattice relaxation time T_1 was determined at several different temperatures in the 7–50 K range by means of an inversion recovery pulse sequence. Experimental curves and monoexponential fits at various temperatures are shown in Figure 4c. The obtained T_1 values are reported as a function of temperature in Figure 4d and Table 1, together with T_m . Similarly, the relaxation times of PTEMPO in frozen solution, obtained by fitting of the experimental data with mono- and biexponential decay functions, respectively (Figure S5, Supporting Information), are included in Figure 4d and Table 1 for comparison. The T_1 times determined for the TEMPO SAM are essentially the same as those for the fast component found for PTEMPO in frozen solution. The slow component of the latter is about a factor of 3–4 slower. The

Table 1. Relaxation times T_1 and T_m of the TEMPO SAM and PTEMPO in frozen solution obtained by an exponential fit of the experimental data. For the TEMPO SAM a monoexponential model was used, except for T_m at 10 and 20 K where a stretched exponential decay was necessary. The PTEMPO data were fitted using a biexponential and a monoexponential model for T_1 and T_m , respectively.

T [K]	TEMPO SAM T_1 [ms]	PTEMPO $T_{1,slow}$ [ms]	PTEMPO $T_{1,fast}$ [ms]	PTEMPO $\chi_{T1,slow}$ [%]	TEMPO SAM T_m [μ s]	TEMPO SAM x	PTEMPO T_m [μ s]
7	–	87(2)	21(1)	50(2)	–	–	2.84(2)
10	9.2(6)	57(1)	14.4(6)	52(1)	13.53(7)	1.85(5)	3.23(3)
20	3.6(5)	25.7(6)	6.2(4)	62(2)	12.81(8)	1.77(5)	3.10(3)
30	1.5(2)	13.0(4)	3.5(3)	62(8)	7.24(4)	1	2.97(3)
40	0.5(1)	4.2(1)	1.2(1)	65(3)	6.83(5)	1	3.19(3)
50	0.3(1)	2.00(7)	0.69(6)	60(4)	5.86(5)	1	3.40(3)
60	–	1.00(4)	0.37(4)	66(5)	6.7(1)	1	2.29(2)

temperature dependence of T_1 for PTEMPO can be well reproduced considering the sum of a direct relaxation mechanism, dominating at low temperatures, and a local vibrational mode of energy 50(7) cm^{-1} dominating at higher temperatures (Equation (S2) and Figure S6, Supporting Information).^[88] Attempts to fit the temperature dependence of T_1 with a Raman process did not provide satisfactory results (Equation (S3) and Figure S7, Supporting Information). The presence of low-energy vibrational modes was confirmed by far infrared spectroscopic measurements of PTEMPO between 30 and 350 cm^{-1} (Figure S8, Supporting Information), where the lowest-energy peak is observed at 62.5 cm^{-1} and the second one at 100 cm^{-1} . These measurements were complemented by DFT calculations (Figure S8 and Table S4, Supporting Information) revealing the first vibrational frequencies at 22.3 cm^{-1} (twisting), 62.5 cm^{-1} (wagging and stretching, including the N–O bond) and 101.5 cm^{-1} (out of plane ring deformation). The energy value found in the fitting process is most likely a combination of these low-lying vibrational modes, however an estimation of the weight of each vibration to the spin relaxation is currently possible only by ab initio calculation of the spin-phonon coupling.^[89] The very similar temperature dependence of T_1 of the TEMPO SAM with respect to PTEMPO indicates that the relaxation mechanisms are probably the same for both samples. This provides a direct proof for the importance of local vibrational modes in the relaxation of paramagnetic molecular species. The T_m values for both TEMPO SAM and PTEMPO samples are largely temperature-independent up to the maximum experimental temperature of 60 K. These values for the TEMPO SAM range from 6 to 13 μ s, depending on temperature, which is rather respectable for molecular qubits, demonstrating the feasibility of the SAM approach to creating functional 2D arrays of molecular qubits. Literature values of T_m for MSQs are usually of a few microseconds at low temperatures and can increase by up to two orders of magnitude by high dilutions of the sample, by removing all nuclear spins in the matrix or by exploiting clock transitions. It is important to note that T_m values of the order of 10 μ s were reported only for significantly diluted qubits (100–10 000 times).^[18,19,42] In contrast, for the TEMPO SAM, a T_m of 6–13 μ s is observed at the dense qubit packing; in fact the CW-EPR measurements reveal the presence of a molecular interaction network. Surprisingly, the T_m values for the TEMPO SAM are 3–4 times longer than for PTEMPO, which is even prepared as a diluted solution. This difference could be tentatively attributed to strong spin-exchange

interactions that reduce decoherence as demonstrated for spin chains.^[90] An alternative explanation lies in the 2D nature of the TEMPO SAM that limits the dimensions of the nuclear spin bath whose dynamics causes electron spin decoherence.

3. Conclusions and Outlook

We have reported a new approach for assembling molecular qubits on surfaces while preserving quantum coherence times. The qubits, represented by the TEMPO radicals, are assembled and decoupled from the surface by using a two-steps strategy: first, the surface is covered by a monolayer of alkanethiolate linkers bearing the click-ready azide groups and, subsequently, the qubits are clicked to the linkers. The spin–lattice relaxation times of the assembled 2D TEMPO array are nearly equal to those of PTEMPO in frozen solution, suggesting local vibrational modes to be the dominant relaxation mechanism. Investigation of the role of spin-phonon coupling in molecular spin qubits is currently a hot-topic and the extension of the recently developed computational techniques to samples such as the TEMPO SAM will certainly contribute to elucidate spin–lattice dynamics in such systems.^[46,89,91,92] Phase memory times measured in a temperature range of 10–60 K varied from 13 to 6 μ s. These values are relatively long compared with those of other molecular spin qubits and, to the best of our knowledge, are the longest reported so far for a non-magnetically diluted system. We are currently investigating in detail the role of exchange interaction on the coherence times.

The above results demonstrate the validity of the proposed fabrication strategy for the realization of functional surface 2D arrays of spin qubits and show that molecular qubits assembled on surfaces can retain their quantum properties. The proposed method is versatile, since it allows for the introduction of a broad range of relevant chemical species by exploiting click chemistry reactions. In principle, any molecule functionalized with a terminal alkyne group can be clicked to the azide-bearing SAM. Consequently, we can imagine of anchoring established molecular spin qubits that feature outstanding quantum properties, such as long coherence times, multilevel structure, ease of addressing the individual spin states, etc. In addition to that, the click reaction approach can be further extended as schematically shown in **Figure 5**. For example, the inclusion of a molecular layer working as a switch and a further qubit layer

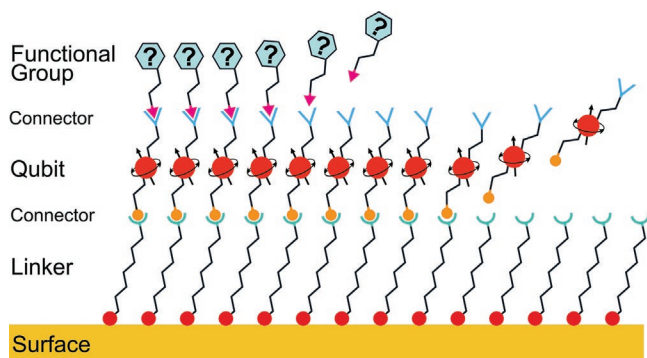


Figure 5. Conceptual scheme of a multilayer modular platform on the basis of a functionalized array of molecular spin qubits. The layers are prepared in consecutive steps: first the linker SAM is assembled, second, the functionalized qubit layer is coupled to the linker through click chemistry, and finally, an additional functional group is grafted to the qubit-terminated SAM.

could allow to assemble a quantum register step by step by a bottom-up approach, fully exploiting the potential of the combination of molecular self-assembly and synthetic chemistry.

4. Experimental Section

Synthesis: The linker molecule 11-azidoundecane-1-thiol (11AUIT) and PTEMPO (4-propargyl-2,2,6,6-tetramethylpiperidine-1-oxyl) were custom-synthesized following literature procedures.^[64,93]

Sample Preparation: Substrates were prepared by subsequent evaporation of 5 nm Cr adhesion layer and a 50 nm gold layer on 125 μm Kapton films. They were cleaned using sonication for 3 min in consecutive baths of demineralized water, isopropyl alcohol and acetone. The substrate was then transferred into a glovebox. For the preparation of the Linker SAM, 980 μL of THF and 20 μL of a 50×10^{-3} M 11-azidoundecane-1-thiol solution in EtOH were mixed and hand-stirred for a few minutes. After 48 h of reaction time, the sample was taken out of the glovebox and sonicated for 3 min in consecutive baths of the mother liquor and fresh EtOH (two times) and then washed copiously with EtOH. The sample was vacuum-dried for 2 h in a desiccator and immediately transferred into a glovebox. For the preparation of TEMPO SAM, the Linker SAM was placed in a 1 mL solution of 1×10^{-3} M 4-propargyl-2,2,6,6-tetramethylpiperidine-1-oxyl (PTEMPO), 20×10^{-3} M triethylamine, 0.05×10^{-3} M CuI and 0.06×10^{-3} M tris[1-(benzyl-1H-1,2,3-triazol-4-yl)methyl]amine (TBTA) in THF and thoroughly hand-stirred for proper mixing for a few minutes. After 6 days of reaction time, the sample was taken out and sonicated for 3 min in consecutive baths of the mother liquor and fresh THF (two times) and then washed copiously with THF. Finally, the sample was vacuum-dried for 2 h in a desiccator and then used for the experiments. In between the experiments, the samples were stored in glovebox.

Atomic Force Microscopy: The images were taken with a Bruker Dimension Icon instrument in tapping mode. AFM images were processed with the instrument software to correct the baseline and they were analyzed using Gwyddion software.^[12]

Polarization-Modulation Infrared Reflection Absorption Spectroscopy: The spectra were recorded on a Bruker VERTEX 70v FT-IR spectrometer equipped with a PMA50 extension module for PM-IRRA spectroscopy. The PM-100 module from Hinds Instruments, Inc. was used as photoelastic modulator and was kept at a $\lambda/2$ retardation with the second harmonic frequency of 84.264 kHz. All spectra were recorded on the freshly prepared samples. The wavenumber setting of the PM was set at 2900 cm^{-1} for the spectra region of 3800–2500 and 2050 cm^{-1} for the spectra region of 2500–1850 and at 1500 cm^{-1} for the spectra region of 1850–800 cm^{-1} . Data analysis was performed with the in-built software

OPUS to remove the Bessel baseline. To avoid artifacts due to bending of the Kapton substrate, a metal vacuum chuck with multiple holes was designed, fabricated and used.

X-ray Photoelectron Spectroscopy and Near-Edge X-ray Absorption Fine Structure Spectroscopy: XPS and NEXAFS spectroscopy measurements were carried out at the HE-SGM beamline (bending magnet) of the synchrotron storage ring BESSY II in Berlin. This beamline provides linearly polarized light with a polarization factor of $\approx 90\%$. A custom-designed experimental station was used.^[94] All measurements were carried out in UHV, at a base pressure of $\approx 1 \times 10^{-9}$ mbar and room temperature. The XPS spectra were measured with a Scienta R3000 electron energy analyzer, in normal emission geometry. The primary photon energy was varied depending on the acquisition range. The binding energy scale was referenced to the Au $4f_{7/2}$ emission at 84.0 eV.^[95] The NEXAFS spectra were measured at both C and N K-edges in the partial electron yield acquisition mode with a retarding voltage of -150 and -300 V, respectively. The energy resolution was ≈ 0.3 and ≈ 0.45 eV, respectively. The photon energy scale was referenced to the pronounced π^* resonance of highly oriented pyrolytic graphite at 285.38 eV.^[96] Raw NEXAFS spectra were corrected for the photon energy dependence of the primary X-ray flux and reduced to the standard form.^[73]

Only most representative and relevant data are shown, e.g., for the N K-edge only in the case of NEXAFS spectroscopy. Note that the efficiency of the click reaction was additionally verified by clicking ferrocene on Au/Si^[97] and 1-ethynyl-3,5-bis(trifluoromethyl)benzene (CF₃Ph) to the 11AUIT SAM prepared on Au/Kapton in the same fashion as in the case of PTEMPO. This molecule features $-\text{CF}_3$ groups, which can be traced by C 1s XPS, and phenyl ring, which can be traced by NEXAFS spectroscopy at the C K-edge. According to the data (see Figure S2 in the Supporting Information), the click reaction worked with nearly 100% efficiency, resulting in well-defined CF₃Ph-bearing SAMs.

Cyclic Voltammetry: Cyclic voltammetry measurements were conducted using a 3-electrode setup, where the working electrode is the sample itself, the reference electrode is an AgCl-coated silver wire and the counter electrode is a Pt wire. The electrodes were submerged in an acetonitrile solution with 0.1 M of tetrabutylammonium perchlorate (TBAClO₄) as electrolyte and the cell was filled with Argon. The measurements on the TEMPO SAM on Au/Kapton were performed at room temperature and ambient pressure. The equipment used for these measurements was Metrohm Autolab with NOVA 2.1.4 software.

Electron Paramagnetic Resonance: Continuous wave X-Band EPR measurements were carried out with a Bruker EMX spectrometer using an Oxford Instruments 4102ST continuous flow helium cryostat resonator ($\nu = 9.47$ GHz) for the measurements at room temperature and from 7 to 180 K. In addition, a 4105DR double resonator ($\nu = 9.59$ GHz) cooled with a continuous flow of a cold N₂ stream was employed for the measurements from 150 to 270 K. The TEMPO SAM sample was freshly prepared and cut in four stripes 0.2 cm \times 1 cm and inserted into the EPR tube. Pulsed Q-Band EPR measurements were performed on a home-built spectrometer ($\nu = 35.0$ GHz)^[98] and using a home-built Fabry-Pérot resonator.^[86] For the measurements on TEMPO SAM, four pieces of 7 mm \times 7 mm were placed into the resonator, whereas PTEMPO in frozen solution was measured in a cylindrical resonator. The resonator was inserted into an Oxford Instruments CF9350 continuous flow helium cryostat. The pulse lengths were 40 ns ($\pi/2$) and 80 ns (π). ESE-detected spectra were measured using a Hahn echo pulse sequence ($\pi/2 - \tau - \pi - \tau$ -echo) with fixed $\tau = 350$ ns under sweeping of the magnetic field. The magnetic field offset was corrected according to the X-band g -values. Phase memory times were measured using the same Hahn echo sequence at the magnetic field corresponding to the maximum of the echo-detected spectrum. Spin-lattice relaxation times were measured using the inversion recovery sequence ($\pi - T - \pi/2 - \tau - \pi - \tau$ -echo). All data were analyzed using Easyspin package^[99] on Matlab, as well as Numpy, Scipy, and Matplotlib libraries for Python.

Far-Infrared Spectroscopy: Far-infrared spectroscopy experiments were done using a Vertex Bruker VERTEX 70v FT-IR spectrometer. The measurements were carried out on a pellet of PTEMPO powder

in eicosane matrix, using a pellet of pure eicosane as a background reference. Fabry–Pérot interference within the pellet created oscillations in the spectrum below 100 cm^{-1} . Therefore, a second sample was prepared by placing a uniform layer of a ground powder sample of PTEMPO on TESA transparent tape and using the pristine tape as a background reference.

Density Functional Theory: Calculations of the vibrational modes of PTEMPO were done in ORCA 4.2.1 using a DFT level of theory.^[100] The initial geometry was optimized starting from the crystal structure and using the D3BJ correction.^[101] The functional was B3LYP with def2-TZVP basis set and def2// auxiliary basis set.^[102,103] The output vibrations were altogether rescaled by multiplying by a factor 1.22.

Supporting Information

Supporting Information is available from the Wiley Online Library or from the author.

Acknowledgements

This research was supported by the Deutsche Forschungsgemeinschaft (DFG, German Research Foundation) – Project-ID 358283783 – SFB 1333, DFG INST 41/999-1, the Center for Integrated Quantum Science and Technology (IQST), the Carl-Zeiss Foundation, the BW Foundation (Competence Network Quantum Technology, project QT5). S.D. and M.Z. thank the Helmholtz Zentrum Berlin for the allocation of synchrotron radiation beamtime at BESSY II and financial support. The authors acknowledge David Neußer, David Hunger, Jonathan Wischnat, Katja Drerup, Sally Eickmeier and Dr. Dominik Bloos for their help with the experimental work.

Open access funding enabled and organized by Projekt DEAL.

Conflict of Interest

The authors declare no conflict of interest.

Data Availability Statement

The data that support the findings of this study are available from the corresponding author upon reasonable request.

Keywords

click chemistry, electron paramagnetic resonance, modular platforms, quantum bits, qubits, self-assembled monolayers, TEMPO

Received: September 29, 2022

Revised: November 30, 2022

Published online: January 22, 2023

- [1] R. P. Feynman, *Int. J. Theor. Phys.* **1982**, 21, 467.
 [2] S. A. Iyengar, A. B. Puthirath, V. Swaminathan, *Adv. Mater.* **2022**, <https://doi.org/10.1002/adma.202107839>.
 [3] S. McArdle, S. Endo, A. Aspuru-Guzik, S. C. Benjamin, X. Yuan, *Rev. Mod. Phys.* **2020**, 92, 015003.
 [4] A. J. Heinrich, W. D. Oliver, L. M. K. Vandersypen, A. Ardavan, R. Sessoli, D. Loss, A. B. Jayich, J. Fernandez-Rossier, A. Laucht, A. Morello, *Nat. Nanotechnol.* **2021**, 16, 1318.

- [5] N. P. Mauranyapin, A. Terrasson, W. P. Bowen, *Adv. Quantum Technol.* **2022**, 5, 2100139.
 [6] M. A. Nielsen, I. L. Chuang, *Quantum Computation and Quantum Information: 10th Anniversary Edition*, Cambridge University Press, Cambridge, UK **2010**.
 [7] N. Gisin, R. Thew, *Nat. Photonics* **2007**, 1, 165.
 [8] F. Arute, K. Arya, R. Babbush, D. Bacon, J. C. Bardin, R. Barends, R. Biswas, S. Boixo, F. G. S. L. Brandao, D. A. Buell, B. Burkett, Y. Chen, Z. Chen, B. Chiaro, R. Collins, W. Courtney, A. Dunsworth, E. Farhi, B. Foxen, A. Fowler, C. Gidney, M. Giustina, R. Graff, K. Guerin, S. Habegger, M. P. Harrigan, M. J. Hartmann, A. Ho, M. Hoffmann, T. Huang, et al., *Nature* **2019**, 574, 505.
 [9] J. Clarke, F. K. Wilhelm, *Nature* **2008**, 453, 1031.
 [10] C. Li, R. Soleyman, M. Kohandel, P. Cappellaro, *Nano Lett.* **2022**, 22, 43.
 [11] J. Meinel, V. Vorobyov, B. Yavkin, D. Dasari, H. Sumiya, S. Onoda, J. Isoya, J. Wrachtrup, *Nat. Commun.* **2021**, 12, 2737.
 [12] A. Chatterjee, P. Stevenson, S. De Franceschi, A. Morello, N. P. de Leon, F. Kuemmeth, *Nat. Rev. Phys.* **2021**, 3, 157.
 [13] C. Koeffel, D. Loss, *Annu. Rev. Condens. Matter Phys.* **2013**, 4, 51.
 [14] A. Browaeys, T. Lahaye, *Nat. Phys.* **2020**, 16, 132.
 [15] R. Blatt, D. Wineland, *Nature* **2008**, 453, 1008.
 [16] A. Alfieri, S. B. Anantharaman, H. Zhang, D. Jariwala, *Adv. Mater.* **2022**, <https://doi.org/10.1002/adma.202109621>.
 [17] N. R. Glavin, P. M. Ajayan, S. Kar, *Adv. Mater.* **2022**, <https://doi.org/10.1002/adma.202109892>.
 [18] M. Atzori, R. Sessoli, *J. Am. Chem. Soc.* **2019**, 141, 11339.
 [19] A. Gaita-Ariño, F. Luis, S. Hill, E. Coronado, *Nat. Chem.* **2019**, 11, 301.
 [20] S. von Kugelgen, D. E. Freedman, *Science* **2019**, 366, 1070.
 [21] D. Loss, D. P. DiVincenzo, *Phys. Rev. A* **1997**, 57, 120.
 [22] E. Moreno-Pineda, W. Wernsdorfer, *Nat. Rev. Phys.* **2021**, 3, 645.
 [23] C. Godfrin, A. Ferhat, R. Ballou, S. Klyatskaya, M. Ruben, W. Wernsdorfer, F. Balestro, *Phys. Rev. Lett.* **2017**, 119, 187702.
 [24] M. Mannini, F. Pineider, P. Sainctavit, C. Danieli, E. Otero, C. Sciancalepore, A. M. Talarico, M. A. Arrio, A. Cornia, D. Gatteschi, R. Sessoli, *Nat. Mater.* **2009**, 8, 194.
 [25] A. Urtizberea, E. Natividad, P. J. Alonso, L. Pérez-Martínez, M. A. Andrés, I. Gascón, I. Gimeno, F. Luis, O. Roubeau, *Mater. Horiz.* **2020**, 7, 885.
 [26] M. Atzori, A. Chiesa, E. Morra, M. Chiesa, L. Sorace, S. Carretta, R. Sessoli, *Chem. Sci.* **2018**, 9, 6183.
 [27] F. Luis, P. J. Alonso, O. Roubeau, V. Velasco, D. Zueco, D. Aguilà, J. I. Martínez, L. A. Barrios, G. Aromí, *Commun. Chem.* **2020**, 3, 176.
 [28] G. A. Timco, S. Carretta, F. Troiani, F. Tuna, R. J. Pritchard, C. A. Muryn, E. J. L. McInnes, A. Ghirri, A. Candini, P. Santini, G. Amoretti, M. Affronte, R. E. P. Winpenny, *Nat. Nanotechnol.* **2009**, 4, 173.
 [29] S. Carretta, D. Zueco, A. Chiesa, Gómez-León, F. L., *Appl. Phys. Lett.* **2021**, 118, 240501.
 [30] M. Warner, S. Din, I. S. Tupitsyn, G. W. Morley, A. M. Stoneham, J. A. Gardener, Z. Wu, A. J. Fisher, S. Heutz, C. W. M. Kay, G. Aeppli, *Nature* **2013**, 503, 504.
 [31] M. Kern, L. Tesi, D. Neusser, N. Rußegger, M. Winkler, A. Allgaier, Y. M. Gross, S. Bechler, H. S. Funk, L. Te Chang, J. Schulze, S. Ludwigs, J. van Slageren, *Adv. Funct. Mater.* **2021**, 31, 2006882.
 [32] L. Tesi, E. Lucaccini, I. Cimatti, M. Perfetti, M. Mannini, M. Atzori, E. Morra, M. Chiesa, A. Caneschi, L. Sorace, R. Sessoli, *Chem. Sci.* **2016**, 7, 2074.
 [33] M. Atzori, E. Morra, L. Tesi, A. Albino, M. Chiesa, L. Sorace, R. Sessoli, *J. Am. Chem. Soc.* **2016**, 138, 11234.
 [34] M. Shiddiq, D. Komijani, Y. Duan, A. Gaita-Ariño, E. Coronado, S. Hill, *Nature* **2016**, 531, 348.
 [35] L. Escalera-Moreno, J. J. Baldoví, A. Gaita-Ariño, E. Coronado, *Chem. Sci.* **2018**, 9, 3265.
 [36] C. J. Yu, S. Von Kugelgen, M. D. Krzyaniak, W. Ji, W. R. Dichtel, M. R. Wasielewski, D. E. Freedman, *Chem. Mater.* **2020**, 32, 10200.

- [37] S. Chicco, A. Chiesa, G. Allodi, E. Garlatti, M. Atzori, L. Sorace, R. De Renzi, R. Sessoli, S. Carretta, *Chem. Sci.* **2021**, *12*, 12046.
- [38] M. J. Amdur, K. R. Mullin, M. J. Waters, D. Puggioni, M. K. Wojnar, M. Gu, L. Sun, P. H. Oyala, J. M. Rondinelli, D. E. Freedman, *Chem. Sci.* **2022**, *13*, 7034.
- [39] A. Lunghi, S. Sanvito, *Sci. Adv.* **2019**, *5*, eaax7163.
- [40] S. L. Bayliss, D. W. Laorenza, P. J. Mintun, B. D. Kovos, D. E. Freedman, D. D. Awschalom, *Science* **2020**, *370*, 1309.
- [41] D. Serrano, S. K. Kuppusamy, B. Heinrich, O. Fuhr, D. Hunger, M. Ruben, P. Goldner, *Nature* **2022**, *603*, 241.
- [42] K. Kundu, J. R. K. White, S. A. Moehring, J. M. Yu, J. W. Ziller, F. Furche, W. J. Evans, S. Hill, *Nat. Chem.* **2022**, *14*, 392.
- [43] J. M. Zadrozny, J. Niklas, O. G. Poluektov, D. E. Freedman, *ACS Cent. Sci.* **2015**, *1*, 488.
- [44] K. Bader, D. Dengler, S. Lenz, B. Endeward, S. D.a Jiang, P. Neugebauer, J. van Slageren, *Nat. Commun.* **2014**, *5*, 5304.
- [45] M. Atzori, L. Tesi, E. Morra, M. Chiesa, L. Sorace, R. Sessoli, *J. Am. Chem. Soc.* **2016**, *138*, 2154.
- [46] A. Chiesa, F. Cugini, R. Hussain, E. MacAluso, G. Allodi, E. Garlatti, M. Giansiracusa, C. A. P. Goodwin, F. Ortu, D. Reta, J. M. Skelton, T. Guidi, P. Santini, M. Solzi, R. De Renzi, D. P. Mills, N. F. Chilton, S. Carretta, *Phys. Rev. B* **2020**, *101*, 174402.
- [47] A. Chiesa, F. Petiziol, M. Chizzini, P. Santini, S. Carretta, *J. Phys. Chem. Lett.* **2022**, *13*, 6468.
- [48] S. J. Lockyer, A. Chiesa, G. A. Timco, E. J. L. McInnes, T. S. Bennett, I. J. Vitorica-Yezebal, S. Carretta, R. E. P. Winpenny, *Chem. Sci.* **2021**, *12*, 9104.
- [49] J. Liu, J. Mrozek, W. K. Myers, G. A. Timco, R. E. P. Winpenny, B. Kintzel, W. Plass, A. Ardavan, *Phys. Rev. Lett.* **2019**, *122*, 37202.
- [50] M. Mayländer, S. Chen, E. R. Lorenzo, M. R. Wasielewski, S. Richert, *J. Am. Chem. Soc.* **2021**, *143*, 7050.
- [51] W. Wernsdorfer, M. Ruben, *Adv. Mater.* **2019**, *31*, 1806687.
- [52] Y. X. Wang, Z. Liu, Y. H. Fang, S. Zhou, S. D.a Jiang, S. Gao, *npj Quantum Inf.* **2021**, *7*, 32.
- [53] C. Bonizzoni, A. Ghirri, K. Bader, J. Van Slageren, M. Perfetti, L. Sorace, Y. Lan, O. Fuhr, M. Ruben, M. Affronte, *Dalt. Trans.* **2016**, *45*, 16596.
- [54] C. Bonizzoni, A. Ghirri, F. Santanni, M. Atzori, L. Sorace, R. Sessoli, M. Affronte, *npj Quantum Inf.* **2020**, *6*, 68.
- [55] I. Gimeno, W. Kersten, M. C. Pallarés, P. Hermosilla, M. J. Martínez-Pérez, M. D. Jenkins, A. Angerer, C. Sánchez-Azqueta, D. Zueco, J. Majer, A. Lostao, F. Luis, *ACS Nano* **2020**, *14*, 8707.
- [56] I. Cimatti, L. Bondi, G. Serrano, L. Malavolti, B. Cortigiani, E. Velez-Fort, D. Betto, A. Ouerghi, N. B. Brookes, S. Loth, M. Mannini, F. Totti, R. Sessoli, *Nanoscale Horiz.* **2019**, *4*, 1202.
- [57] G. Serrano, L. Poggini, M. Briganti, A. L. Sorrentino, G. Cucinotta, L. Malavolti, B. Cortigiani, E. Otero, P. Sainctavit, S. Loth, F. Parenti, A. L. Barra, A. Vindigni, A. Cornia, F. Totti, M. Mannini, R. Sessoli, *Nat. Mater.* **2020**, *19*, 546.
- [58] L. Poggini, A. Lunghi, A. Collauto, A. Barbon, L. Armelao, A. Magnani, A. Caneschi, F. Totti, L. Sorace, M. Mannini, *Nanoscale* **2021**, *13*, 7613.
- [59] G. Rajaraman, A. Caneschi, D. Gatteschi, F. Totti, *J. Mater. Chem.* **2010**, *20*, 10747.
- [60] M. Mas-Torrent, N. Crivillers, C. Rovira, J. Veciana, *Chem. Rev.* **2012**, *112*, 2506.
- [61] J. A. De Sousa, F. Bejarano, D. Gutiérrez, Y. R. Leroux, E. M. Nowik-Boltyk, T. Junghofer, E. Giangrisostomi, R. Ovsyannikov, M. B. Casu, J. Veciana, M. Mas-Torrent, B. Fabre, C. Rovira, N. Crivillers, *Chem. Sci.* **2020**, *11*, 516.
- [62] M. Mannini, L. Sorace, L. Gorini, F. M. Piras, A. Caneschi, A. Magnani, S. Menichetti, D. Gatteschi, *Langmuir* **2007**, *23*, 2389.
- [63] L. Zhang, Y. B. Vogel, B. B. Noble, V. R. Gonçalves, N. Darwish, A. Le Brun, J. J. Gooding, G. G. Wallace, M. L. Coote, S. Ciampi, *J. Am. Chem. Soc.* **2016**, *138*, 9611.
- [64] R. Yan, L. L.e Pleux, M. Mayor, M. Zharnikov, *J. Phys. Chem. C* **2016**, *120*, 25967.
- [65] H. C. Kolb, M. G. Finn, K. B. Sharpless, *Angew. Chem., Int. Ed.* **2001**, *40*, 2004.
- [66] V. V. Rostovtsev, L. G. Green, V. V. Fokin, K. B. Sharpless, *Angew. Chem., Int. Ed.* **2002**, *41*, 2596.
- [67] J. L. Du, G. R. Eaton, S. S. Eaton, *J. Magn. Reson., Ser. A* **1995**, *115*, 213.
- [68] H. Kobayashi, T. Ueda, K. Miyakubo, T. Eguchi, A. Tani, *Phys. Chem. Chem. Phys.* **2008**, *10*, 1263.
- [69] R. G. Nuzzo, L. H. Dubois, D. L. Allara, *J. Am. Chem. Soc.* **1990**, *112*, 558.
- [70] M. D. Porter, T. B. Bright, D. L. Allara, C. E. Chidsey, *J. Am. Chem. Soc.* **1987**, *109*, 3559.
- [71] A. A. Jbarah, A. Ihle, K. Banert, R. Holze, *J. Raman Spectrosc.* **2006**, *37*, 123.
- [72] E. Darlatt, C. H. H. Traulsen, J. Poppenberg, S. Richter, J. Kühn, C. A. Schalley, W. E. S. Unger, *J. Electron Spectrosc. Relat. Phenom.* **2012**, *185*, 85.
- [73] J. Stöhr, *NEXAFS Spectroscopy*, Springer, Berlin/Heidelberg, Germany, **1992**.
- [74] E. Darlatt, A. Nefedov, C. H. H. Traulsen, J. Poppenberg, S. Richter, P. M. Dietrich, A. Lippitz, R. Illgen, J. Kühn, C. A. Schalley, C. Wöll, W. E. S. Unger, *J. Electron Spectrosc. Relat. Phenom.* **2012**, *185*, 621.
- [75] F. Schreiber, *Prog. Surf. Sci.* **2000**, *65*, 151.
- [76] T. Risse, T. Hill, J. Schmidt, G. Abend, H. Hamann, H. J. Freund, *J. Phys. Chem. B* **1998**, *102*, 2668.
- [77] F. Busolo, L. Franco, L. Armelao, M. Maggini, *Langmuir* **2010**, *26*, 1889.
- [78] P. Krukowski, W. Kozłowski, W. Olejniczak, Z. Klusek, M. Puchalski, P. Dabrowski, P. J. Kowalczyk, K. Gwozdziński, G. Grabowski, *Appl. Surf. Sci.* **2008**, *255*, 1921.
- [79] D. Johnston, R. Kremer, M. Troyer, *Phys. Rev. B* **2000**, *61*, 9558.
- [80] B. C. Keith, C. P. Landee, T. Valleau, M. M. Turnbull, N. Harrison, *Phys. Rev. B* **2011**, *84*, 104442.
- [81] A. Abragam, B. Bleaney, *Electron Paramagnetic Resonance of Transition Ions*, Dover Publications, Inc., Mineola, NY, USA, **1986**.
- [82] A. Bencini, D. Gatteschi, *Electron Paramagnetic Resonance of Exchange Coupled Systems*, Springer, Berlin/Heidelberg, Germany, **1990**.
- [83] V. N. Parmon, A. I. Kokorin, G. M. Zhidomirov, *J. Struct. Chem.* **1977**, *18*, 104.
- [84] G. R. Luckhurst, *Mol. Phys.* **1966**, *10*, 543.
- [85] Y. Kanzaki, D. Shiomi, K. Sato, T. Takui, *J. Phys. Chem. B* **2012**, *116*, 1053.
- [86] S. Lenz, B. Kern, M. Schneider, J. Van Slageren, *Chem. Commun.* **2019**, *55*, 7163.
- [87] S. Lenz, D. König, D. Hunger, J. van Slageren, *Adv. Mater.* **2021**, *33*, 2101673.
- [88] T. Yamabayashi, M. Atzori, L. Tesi, G. Cosquer, F. Santanni, M. E. Boulon, E. Morra, S. Benci, R. Torre, M. Chiesa, L. Sorace, R. Sessoli, M. Yamashita, *J. Am. Chem. Soc.* **2018**, *140*, 12090.
- [89] A. Lunghi, *Sci. Adv.* **2022**, *8*, eabn7880.
- [90] S. Bertaina, C. E. Dutoit, J. Van Tol, M. Dressel, B. Barbara, A. Stepanov, *Phys. Rev. B: Condens. Matter Mater. Phys.* **2014**, *90*, 060404.
- [91] D. Reta, J. G. C. Kragoskow, N. F. Chilton, *J. Am. Chem. Soc.* **2021**, *143*, 5943.
- [92] A. Albino, S. Benci, L. Tesi, M. Atzori, R. Torre, S. Sanvito, R. Sessoli, A. Lunghi, *Inorg. Chem.* **2019**, *58*, 10260.
- [93] X. Wang, J. Huang, L. Chen, Y. Liu, G. Wang, *Macromolecules* **2014**, *47*, 7812.
- [94] A. Nefedov, C. Wöll, *Advanced Applications of NEXAFS Spectroscopy for Functionalized Surfaces*, Springer, Berlin/Heidelberg, Germany, **2013**.
- [95] J. F. Moulder, W. E. Stickle, P. E. Sobol, K. D. Bomben, *Handbook of X-Ray Photoelectron Spectroscopy*, Perkin-Elmer Corp., Eden Prairie, MN, USA, **1992**.

- [96] P. E. Batson, *Phys. Rev. B* **1993**, *48*, 2608.
- [97] J. E. Kuhlmann, S. S. Y. Liu, K. Dirnberger, M. Zharnikov, S. Ludwigs, *Chem. - Eur. J.* **2021**, *27*, 17255.
- [98] I. Tkach, A. Baldansuren, E. Kalabukhova, S. Lukin, A. Sitnikov, A. Tsvir, M. Ischenko, Y. Rosentzweig, E. Roduner, *Appl. Magn. Reson.* **2008**, *35*, 95.
- [99] S. Stoll, A. Schweiger, *J. Magn. Reson.* **2006**, *178*, 42.
- [100] F. Neese, *WIREs Comput. Mol. Sci.* **2012**, *2*, 73.
- [101] S. Grimme, J. Antony, S. Ehrlich, H. Krieg, *J. Chem. Phys.* **2010**, *132*, 154104.
- [102] F. Weigend, R. Ahlrichs, *Phys. Chem. Chem. Phys.* **2005**, *7*, 3297.
- [103] F. Weigend, *Phys. Chem. Chem. Phys.* **2006**, *8*, 1057.